UC Irvine
UC Irvine Previously Published Works

Title
Probing differences among Aβ oligomers with two triangular trimers derived from Aβ

Authors
Kreutzer, Adam G
Guaglianone, Gretchen
Yoo, Stan
et al.

Probing differences among Aβ oligomers with two triangular trimers derived from Aβ

Adam G. Kreutzer[a,1,2] (ID), Gretchen Guaglianone[a,1] (ID), Stan Yoo[a], Chelsea Marie T. Parrocha[b], Sarah M. Ruttenberg[a] (ID), Ryan J. Malonis[c], Karen Tong[c], Yu-Fu Lin[d] (ID), Jennifer T. Nguyen[b] (ID), William J. Howitz[a] (ID), Michelle N. Diab[a], Imane L. Hamza[a], Jonathan R. Lai[c] (ID), Vicki H. Wysocki[d] (ID), and James S. Nowick[a,b,2] (ID)

The assembly of the β-amyloid peptide (Aβ) to form oligomers and fibrils is closely associated with the pathogenesis and progression of Alzheimer's disease. Aβ is a shape-shifting peptide capable of adopting many conformations and folds within the multitude of oligomers and fibrils the peptide forms. These properties have precluded detailed structural elucidation and biological characterization of homogeneous, well-defined Aβ oligomers. In this paper, we compare the structural, biophysical, and biological characteristics of two different covalently stabilized isomorphic trimers derived from the central and *C*-terminal regions Aβ. X-ray crystallography reveals the structures of the trimers and shows that each trimer forms a ball-shaped dodecamer. Solution-phase and cell-based studies demonstrate that the two trimers exhibit markedly different assembly and biological properties. One trimer forms small soluble oligomers that enter cells through endocytosis and activate capase-3/7-mediated apoptosis, while the other trimer forms large insoluble aggregates that accumulate on the outer plasma membrane and elicit cellular toxicity through an apoptosis-independent mechanism. The two trimers also exhibit different effects on the aggregation, toxicity, and cellular interaction of full-length Aβ, with one trimer showing a greater propensity to interact with Aβ than the other. The studies described in this paper indicate that the two trimers share structural, biophysical, and biological characteristics with oligomers of full-length Aβ. The varying structural, assembly, and biological characteristics of the two trimers provide a working model for how different Aβ trimers can assemble and lead to different biological effects, which may help shed light on the differences among Aβ oligomers.

Aβ oligomers | Alzheimer's disease | X-ray crystallography | native mass spectrometry | cellular toxicity

Oligomers of the β-amyloid peptide (Aβ) are central to the pathogenesis and progression of Alzheimer's disease (1–18). Aβ dimers and trimers, as well as higher-order oligomers, such as hexamers and dodecamers and larger oligomers, are thought to have special significance in Alzheimer's disease (19, 20). Aβ plaques from Alzheimer's disease individuals contain cross-linked Aβ dimers that are composed of different Aβ alloforms (21). Aβ dimers appear to be the building blocks of large, mildly cytotoxic oligomers (22). Concentrations of Aβ trimers are elevated in cognitively normal adults who are at risk for Alzheimer's disease (23). Aβ trimers appear to be the building blocks of the putative dodecamer of Aβ, termed Aβ*56, although recent reports have called the identification, characterization, and study of Aβ*56 into question (24–28). Aβ dimers, Aβ trimers, and Aβ*56 promote phosphorylation and aggregation of the microtubule-associated protein tau, which is also involved in Alzheimer's disease progression (29–31).

While cryo-EM and ssNMR spectroscopy have revealed the structures of many Aβ fibrils (32–48), high-resolution structures of Aβ oligomers are largely unknown, and the relationship between Aβ oligomer structure and Aβ oligomer biology is unclear. The challenges of isolating stable biogenic Aβ oligomers of sufficient quantity and homogeneity or preparing homogeneous Aβ oligomers in vitro have precluded detailed characterization of the relationship between the structures and biological properties of Aβ oligomers.

To study Aβ oligomers, researchers have developed a variety of methods for preparing Aβ oligomers in vitro (49–62). Studies of these in vitro preparations have shown that Aβ can form many oligomers that differ in size, stoichiometry, morphology, toxicity, and ability to form fibrils. The formation and properties of these different Aβ oligomers are highly dependent on the conditions under which the oligomers are prepared. To reduce the heterogeneity among Aβ oligomers, researchers have prepared and studied Aβ oligomers that consist of Aβ monomers linked by chemical cross-links (63–69). These studies

Significance

Oligomers of the β-amyloid peptide (Aβ) contribute to neurodegeneration in Alzheimer's disease and are promising targets for therapies against Alzheimer's disease. Understanding the structures and biology of Aβ oligomers is important for understanding the molecular basis of Alzheimer's disease and for developing better therapeutics and diagnostics for the disease. Aβ oligomers are difficult to study because they are heterogeneous and unstable. To gain insights into Aβ oligomers and their role in neurodegeneration, we create, characterize, and compare two different well-defined chemical models of Aβ oligomers composed of different peptide fragments from Aβ that are constrained into β-hairpin conformations.

[1]A.G.K. and G.G. contributed equally to this work.

[2]To whom correspondence may be addressed. Email: akreutze@uci.edu or jsnowick@uci.edu.

have helped determine the importance of different residues in Aβ oligomerization and have demonstrated that different Aβ allo-forms form different oligomers. Although cross-linking Aβ decreases the heterogeneity of Aβ oligomers, cross-linking full-length Aβ has not yet produced structurally homogeneous oligomers amenable to high-resolution structural elucidation. X-ray crystallographic studies of fragments of Aβ and other amyloidogenic peptides and proteins, as well as NMR studies of full-length Aβ, have provided clues about amyloid oligomer structures, showing that many amyloid oligomers contain antiparallel β-sheets and packed hydrophobic cores (70–76).

β-hairpins have emerged as important structural motifs in Aβ oligomers and have also been identified as a component of Aβ fibrils (77–86). β-hairpins are the simplest antiparallel β-sheet, comprising two hydrogen-bonded β-strands connected by a loop. Several Aβ β-hairpins have been described in which the central and *C*-terminal regions of the Aβ peptide comprise the β-strands of the β-hairpin. Härd et al. elucidated the NMR structure of an Aβ β-hairpin bound to an affibody (80). Härd et al. subsequently stabilized Aβ$_{40}$ and Aβ$_{42}$ in a β-hairpin conformation by installing a cross-strand intramolecular disulfide bond and demonstrated that these stabilized Aβ β-hairpins assemble to form soluble oligomers that recapitulate many characteristics of Aβ oligomers (81, 82). Tycko et al. elucidated the cryo-EM structure of an Alzheimer's disease brain-derived Aβ$_{40}$ fibril in which Aβ β-hairpins sandwich an extended core composed of parallel β-sheets (86). Yu et al. used NMR spectroscopy to characterize the structure of an Aβ$_{42}$ dimer that contains two Aβ β-hairpins (83). Carulla et al. described the NMR structures of an Aβ tetramer and octamer, which contain Aβ β-hairpins, in a membrane-mimicking lipid bilayer (84, 85).

The alignments of the β-strands from central and *C*-terminal regions of Aβ differ among the β-hairpins described above. The β-strand alignment within an Aβ β-hairpin is significant because different β-strand alignments have different residue pairings, which leads to variations in the surfaces of the β-hairpin on which the amino acid side chains are displayed. *SI Appendix,* Fig. S1 illustrates the five Aβ β-hairpins described in the preceding paragraph and shows how the relationship between two residues—E$_{22}$ and I$_{31}$—varies among these different alignments. We have previously observed that Aβ β-hairpins with different β-strand alignments assemble to form different oligomers with unique three-dimensional structures (87, 88, 89), and we envision that these different oligomers contribute to the structural and biological differences among Aβ oligomers in Alzheimer's disease (20).

To study oligomers composed of Aβ β-hairpins with different β-strand alignments, we have developed the following approach: 1) design and synthesize macrocyclic β-hairpin peptides containing two Aβ β-strands that are constrained into a specific alignment, 2) elucidate the structures of the oligomers that the Aβ β-hairpin peptides form using X-ray crystallography, 3) design and synthesize covalently stabilized Aβ oligomer models, and 4) study the structural, biophysical, and biological properties of the Aβ oligomer models (90, 91). Through this approach, we aim to understand whether different Aβ oligomer models exhibit different structural, biophysical, and biological properties and determine whether these models share characteristics with oligomers of full-length Aβ.

This paper reports the structural, biophysical, and biological characterization of the Aβ oligomer models 2AT and KLT, which are covalently stabilized isomorphic triangular trimers. 2AT is composed of β-hairpin peptides that mimic an Aβ$_{17–36}$ β-hairpin, while KLT is composed of β-hairpin peptides that mimic an Aβ$_{16–36}$ β-hairpin (Fig. 1). Although 2AT and KLT appear morphologically similar, they differ in the arrangement of their component β-hairpin peptides: in 2AT, Aβ$_{30–36}$ constitutes the three
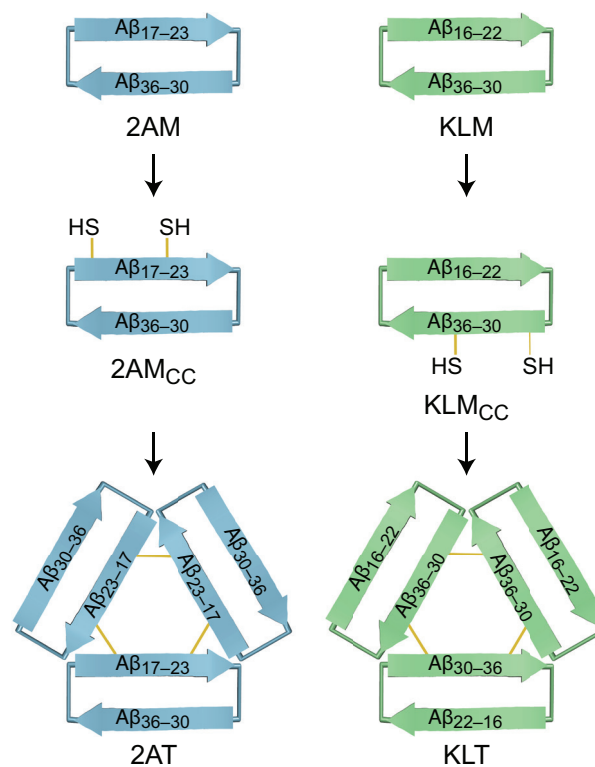

Fig. 1. Design of triangular trimers 2AT and KLT from the β-hairpin peptide monomers 2AM and KLM. *SI Appendix,* Fig. S2 shows the chemical structure of each compound.

outer β-strands of the trimer; in KLT, Aβ$_{30–36}$ constitutes the three inner β-strands of the trimer. Furthermore, the surfaces of 2AT and KLT differ markedly, because of the different arrangement and β-strand alignments of the component β-hairpin peptides. The studies described below show that 2AT and KLT also exhibit markedly different biophysical and biological properties and may thus reflect the types of differences that occur among oligomers of full-length Aβ.

Results and Discussion

Aβ β-Hairpin Peptides 2AM and KLM. We previously reported the design and study of the Aβ β-hairpin peptides 2AM and KLM, which mimic Aβ β-hairpins with different β-strand alignments (87, 92). 2AM mimics an Aβ β-hairpin in which an Aβ$_{17–23}$ β-strand is across from an Aβ$_{30–36}$ β-strand (*SI Appendix,* Fig. S3*A*) similar to the Aβ$_{17–36}$ β-hairpin elucidated by Härd et al. (*SI Appendix,* Fig. S1); KLM mimics an Aβ β-hairpin in which an Aβ$_{16–22}$ β-strand is across from an Aβ$_{30–36}$ β-strand (*SI Appendix,* Fig. S3*C*) similar to the Aβ$_{16–36}$ β-hairpin reported by Tycko et al. (*SI Appendix,* Fig. S1). While 2AM and KLM are designed to mimic the Aβ$_{17–36}$ and Aβ$_{16–36}$ β-hairpins elucidated by Härd et al. and Tycko et al., 2AM and KLM could also serve as models for β-hairpins formed by p3, an amyloid precursor protein cleavage product composed of Aβ residues 17 to 40 known to form oligomers (93).

KLM is an analogue of 2AM in which the top β-strand has shifted by one residue. A comparison of *SI Appendix,* Figs. S3 *B* and *D* illustrates the consequences of shifting the β-strand alignment by one residue. In 2AM, L$_{17}$ pairs with V$_{36}$ and occupies the same surface as V$_{36}$. In KLM, K$_{16}$ is added to the top strand and now pairs with V$_{36}$, and L$_{17}$ now occupies the opposite surface of V$_{36}$ and pairs with M$_{35}$. The β-strands of 2AM and KLM are linked together using the β-turn mimic δ-amine-linked ornithine (94). 2AM and KLM also contain *N*-methyl groups to limit uncontrolled aggregation: in 2AM,

the N-methyl group is on F_{20}; in KLM, the N-methyl group is on G_{33}. 2AM contains an ornithine residue at position 35 instead of the native methionine. Ornithine is a charged isostere of methionine that helps solubilize the peptide. We have shown that a variant of 2AM with the native methionine at position 35 assembles in the crystal state in the same fashion as 2AM (87).

X-ray crystallography revealed that 2AM and KLM fold to form twisted β-hairpins that assemble to form different triangular trimers (*SI Appendix,* Figs. S3 *E* and *F*). (For the X-ray crystallographic study of KLM, we used a variant of KLM with a para-iodo group on F_{19} (KLM$_I$) to facilitate phase determination.) In the triangular trimer formed by 2AM, Aβ$_{30–36}$ constitutes the three outer β-strands of the trimer, whereas in the triangular trimer formed by KLM$_I$, Aβ$_{30–36}$ constitutes the three inner β-strands of the trimer. The triangular trimers formed by 2AM and KLM$_I$ each further assemble to form different dodecamers (*SI Appendix,* Fig. S4). The crystal structures of 2AM and KLM$_I$ demonstrated that Aβ β-strand alignment within β-hairpin peptides can impact the structures of the oligomers that the peptides form. While the triangular trimers formed by 2AM and KLM$_I$ appear similar in morphology, the differing β-strand alignments of their component peptides and the different ways the two peptides assemble to form trimers considerably impact the surfaces of the trimers, which in turn impact the higher-order assembly of the trimers to form dodecamers.

Design and Synthesis of the Covalently Stabilized Triangular Trimers 2AT and KLT. While 2AM and KLM assemble to form triangular trimers at the millimolar concentrations of X-ray crystallography, they do not appear to form triangular trimers at low micromolar concentrations, which are more biologically relevant (95). For this reason, covalent stabilization of the triangular trimers is needed to study their structural, biophysical, and biological properties outside of the crystal lattice. Covalent stabilization of the triangular trimers also ensures oligomer homogeneity, eliminating the monomer-oligomer equilibria that would occur for monomers that assemble to form trimers or other oligomers. We previously stabilized the triangular trimer formed by 2AM by installing disulfide bonds at the three corners of the trimer to create 2AT (96). This was achieved by mutating L_{17} and A_{21} of 2AM to cysteine to yield the peptide 2AM$_{CC}$, which is then oxidized to form 2AT (Fig. 1 and *SI Appendix,* Fig. S2).

We have now designed and synthesized the covalently stabilized triangular trimer KLT, which mimics a triangular trimer formed by KLM (Fig. 1 and *SI Appendix,* Fig. S2). At the three corners of a triangular trimer formed by KLM, A_{30} of one monomer subunit is paired with L_{34} of an adjacent monomer subunit. To stabilize KLM into a triangular trimer and thus create KLT, we mutated A_{30} and L_{34} to cysteine to create KLM$_{CC}$ and then oxidized KLM$_{CC}$ in aqueous DMSO to introduce disulfide cross-links. LC/MS analysis of the crude oxidation reaction mixture reveals that KLM$_{CC}$ forms four major species: KLT, two distinct bis-disulfide cross-linked dimers, and a monomer with an intramolecular disulfide bond (*SI Appendix,* Fig. S5). KLT is isolated from the crude reaction mixture using reverse-phase HPLC to yield 3 to 6 mg of KLT with >98% purity from the oxidation of ~30 mg of KLM$_{CC}$.

Crystal Structures of 2AT and KLT. To investigate the structures of 2AT and KLT, we turned to X-ray crystallography. We previously reported the crystal structure of 2AT (Fig. 2*A*, PDB 5SUR) (95) and now report the crystal structure of KLT (Fig. 2*F*, PDB 8ECA). The X-ray crystallographic phases for KLT were determined by first synthesizing a variant of KLT with a para-iodo group on F_{19} (KLT$_I$) and using SAD phasing to determine the structure of KLT$_I$ and then using the structure of KLT$_I$ as a search model in

molecular replacement. This approach succeeded in determining the phases for KLT because the crystal structure of KLT$_I$ has the same space group and unit cell dimensions as the crystal structure of KLT. *SI Appendix,* Fig. S6 shows the asymmetric units of the crystal structures of KLT and KLT$_I$, which both contain two copies of their respective trimers.

The crystal structures of 2AT and KLT show that the surfaces of both trimers are largely hydrophobic and differ markedly in the arrangement of residues displayed on each surface. A comparison of Fig. 2 *B* and *G* best illustrates the differences between the surfaces of 2AT and KLT. Chief among these differences are the positions of F_{19} and F_{20} and I_{31} and I_{32}. F_{19} and F_{20} occupy the central region of each surface of 2AT, and I_{31} and I_{32} occupy peripheral regions (Fig. 2*B*). I_{31} and I_{32} occupy central regions of KLT, and F_{19} and F_{20} occupy peripheral regions (Fig. 2*G*). Other amino acids shared by both trimers, such as V_{18} and V_{36}, also occupy different positions on the surfaces of 2AT and KLT. The differences in the surfaces of 2AT and KLT result directly from the arrangement of the component β-hairpins of each trimer, as well as the alignment of the β-strands in the component β-hairpin peptides.

Hydrophobic packing between the surfaces of the trimers leads to higher-order assembly of 2AT and KLT in the crystal lattice. We previously reported that four copies of 2AT assemble to form a ball-shaped dodecamer (Fig. 2 *C–E*) (95). The crystal structure of KLT reveals that four copies of KLT also assemble to form a ball-shaped dodecamer (Fig. 2 *H–J*). Although the dodecamers formed by 2AT and KLT are nearly identical in morphology, they differ in topology, containing different residues on the insides and outsides of each dodecamer. The ball-shaped dodecamers formed by 2AT and KLT are both stabilized by a hydrophobic core at the center of each dodecamer. In the dodecamer formed by 2AT, V_{18}, F_{20}, and I_{31} fill the hydrophobic core, with a total of 48 amino acid side chains packing within the core (Fig. 2*E*). In the dodecamer formed by KLT, L_{17}, F_{19}, A_{21}, I_{31}, and M_{35} fill the hydrophobic core, with a total of 60 amino acid side chains packing within the core (Fig. 2*J*). The outer surfaces of each dodecamer are also largely hydrophobic and display different residues, with the 2AT dodecamer displaying F_{19}, A_{30}, I_{32}, L_{34}, V_{36}, and the C_{17}-C_{21} disulfide bonds and the KLT dodecamer displaying V_{18}, F_{20}, I_{32}, V_{36}, and the C_{30}-C_{34} disulfide bonds.

Thus, the crystal structures of 2AT and KLT illustrate how the change in design from 2AT to KLT results in differences in structure between the trimers and supramolecular assembly of corresponding dodecamers. These structural differences arise from the differing β-strand alignments of the component peptides and the different orientations of the component peptides that are cross-linked together to form 2AT and KLT. The following sections detail the impacts that these structural differences have on the solution-phase assembly of 2AT and KLT; how 2AT and KLT interact with and affect cells; and the effect of 2AT and KLT on aggregation and biological properties of full-length Aβ$_{42}$.

Biophysical Studies of 2AT and KLT. To investigate the solution-phase assembly and structural properties of 2AT and KLT, we used a suite of techniques including sodium dodecyl sulfate-polyacrylamide gel electrophoresis (SDS-PAGE), circular dichroism (CD) spectroscopy, native mass spectrometry, and mass photometry. At concentrations of 20 to 50 μM and pH 7 to 8, KLT is largely insoluble and forms large aggregates that pellet upon centrifugation, while 2AT is soluble and remains mostly in solution upon centrifugation. Despite the poor solubility of KLT, we performed the biophysical studies on each trimer without centrifugation before analysis.
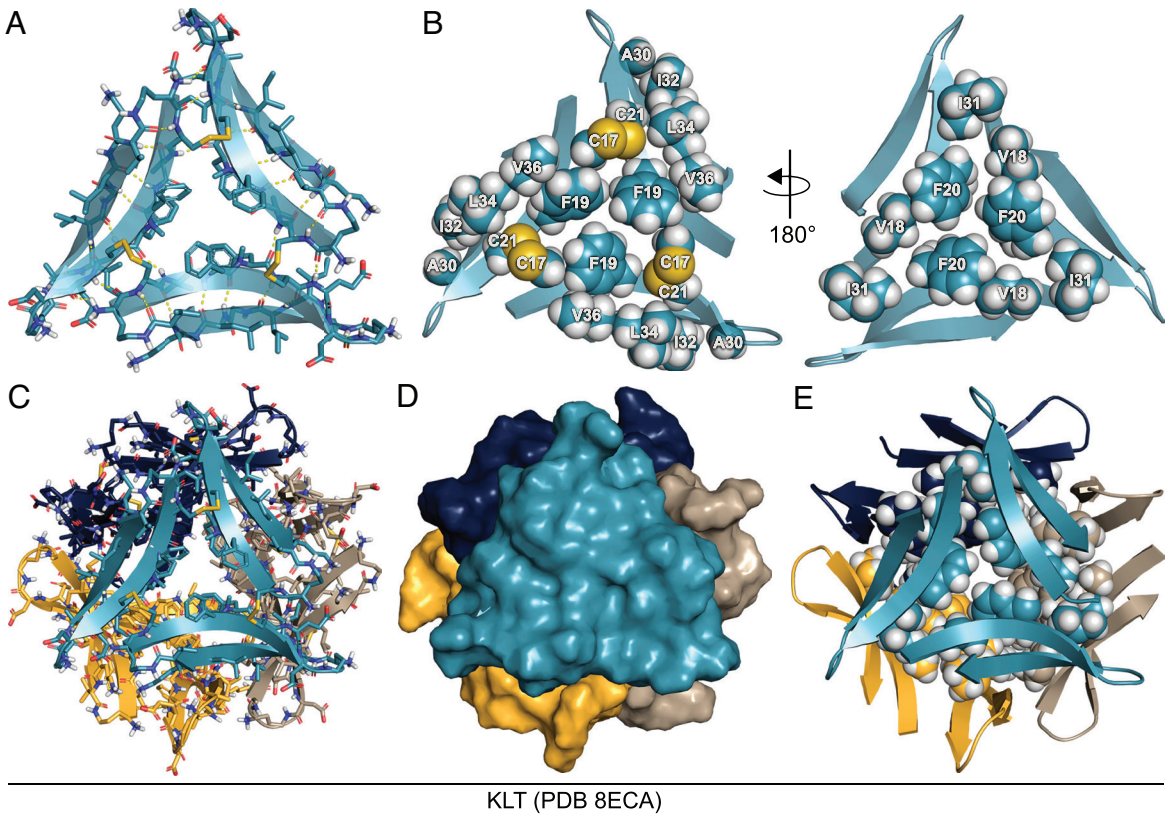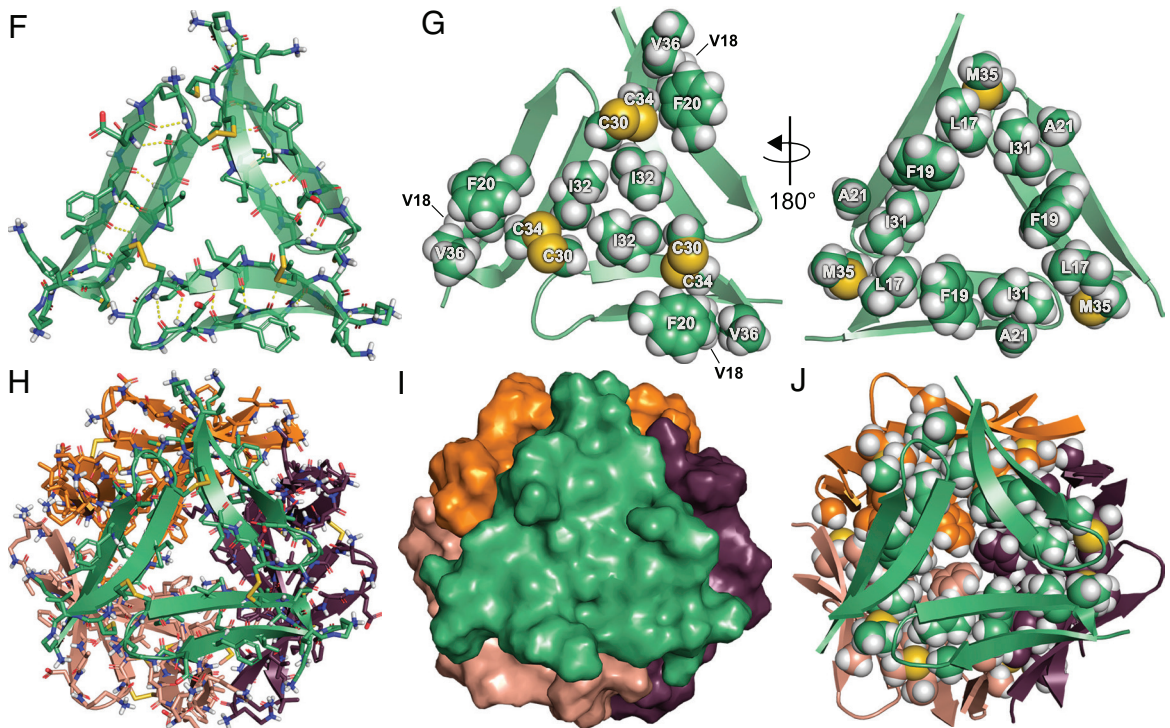
Fig. 2. Crystal structures of 2AT and KLT (PDB 5SUR and 8ECA). (*A*) Cartoon and stick model of 2AT. (*B*) Cartoon and sphere models of 2AT illustrating the two hydrophobic surfaces. (*C*) Cartoon and stick model of the dodecamer formed by 2AT. (*D*) Surface model of the dodecamer formed by 2AT illustrating how the four trimers fit together. (*E*) Cartoon and sphere model of the dodecamer formed by 2AT illustrating the hydrophobic core formed by V_{18}, F_{20}, and I_{31}. (*F*) Cartoon and stick model of KLT. (*G*) Cartoon and sphere models of KLT illustrating the two hydrophobic surfaces. (*H*) Cartoon and stick model of the dodecamer formed by KLT. (*I*) Surface model of the dodecamer formed by KLT illustrating how the four trimers fit together. (*J*) Cartoon and sphere model of the dodecamer formed by KLT illustrating the hydrophobic core formed by L_{17}, F_{19}, A_{21}, I_{31}, and M_{35}.

SDS-PAGE shows that in the lipid environment of SDS, 2AT and KLT exhibit markedly different assembly behavior. In a 16.5% polyacrylamide gel, 2AT migrates as two distinct bands: a band at a molecular weight consistent with a 21.2-kDa dodecamer and a band at a molecular weight consistent with a 5.3-kDa trimer (Fig. 3*A*). The putative dodecamer band formed by 2AT streaks
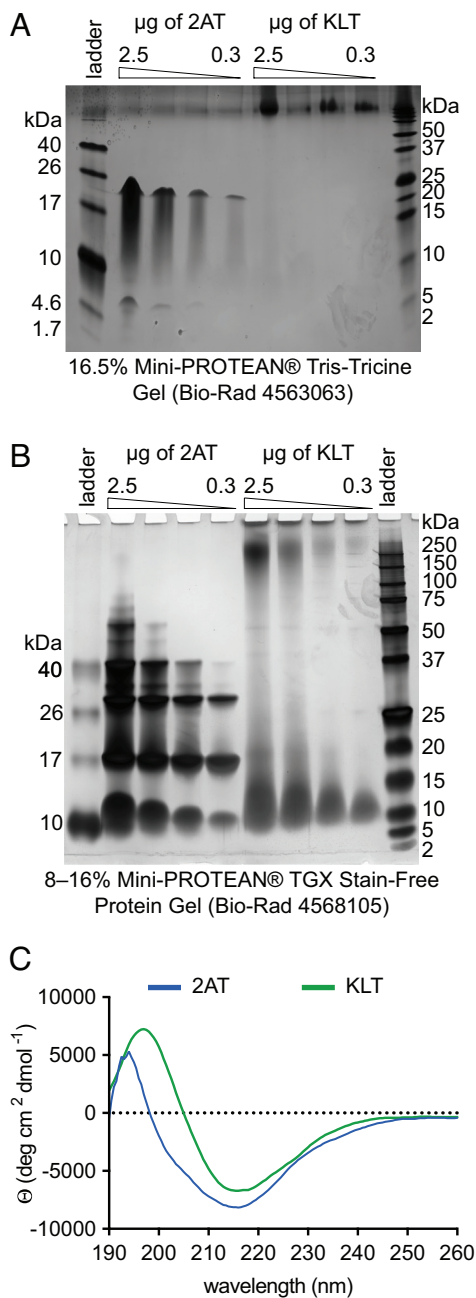
Fig. 3. Biophysical studies of 2AT and KLT. (*A* and *B*) Silver-stained SDS-PAGE of 2AT and KLT. SDS-PAGE samples were prepared in 112.5 mM Tris buffer (pH 8.0) with 2% (w/v) SDS and 6% (v/v) glycerol and then run on a 16.5% polyacrylamide gel (*A*) or an 8–16% polyacrylamide gel (*B*). Both gels were run with Tricine buffer (100 mM Tris base, 100 mM Tricine, and 0.1% (w/v) SDS) at 30 V at 4 °C. (*C*) CD spectra of 2AT and KLT. CD spectra were acquired on 50 μM solutions of 2AT and KLT in 10 mM phosphate buffer (pH 7.4).

downward, suggesting that the dodecamer is in equilibrium with lower-order oligomers, such as hexamers and nonamers. The streaks become fainter at lower concentrations, suggesting that formation of lower-order oligomers by 2AT is concentration dependent; however, this could also reflect the sensitivity of the silver stain. In contrast, KLT does not appear to significantly enter the 16.5% polyacrylamide gel, with most of the trimer entering the stacking gel and then accumulating at the top of the 16.5% running gel as large aggregates (Fig. 3*A*).

To further investigate 2AT and KLT in SDS-PAGE, we also ran the trimers on an 8 to 16% polyacrylamide gel. We found that 2AT exhibits different migration properties in the 8 to 16%

polyacrylamide gel compared to the 16.5% polyacrylamide gel. In the 8 to 16% polyacrylamide gel, 2AT migrates as a series of bands corresponding to small oligomers ranging in size from 1 to 4 or more copies of 2AT, corresponding to trimer, hexamer, nonamer, and dodecamer and larger (Fig. 3*B*). The higher-order oligomer bands at and above the 40-kDa marker band become fainter at lower concentrations, suggesting that the formation of these higher-order oligomers is concentration dependent; however, this could also reflect the sensitivity of the silver stain. The migration differences observed for 2AT between the two different gels may arise from differences in the chemical composition among the two commercially available gels. KLT more substantially enters the 8 to 16% polyacrylamide gel than it does the 16.5% polyacrylamide gel, migrating as bands that correspond to a large aggregate composed of more than fifty copies of KLT and a molecular weight greater than 250 kDa, as well as a lower-molecular-weight band which we interpret to be hexamer or trimer (Fig. 3*B*).

We used CD spectroscopy to better understand the structures and folding of 2AT and KLT in solution. For CD, we prepared 50 μM solutions of 2AT and KLT in phosphate buffer (pH 7.4). The CD spectra of both 2AT and KLT exhibit typical β-hairpin character (97, 98, 99), with minima centered around 216 nm and maxima below 200 nm (Fig. 3*C*). These data support a structural model where the component peptides of 2AT and KLT fold to form β-hairpins in solution. These folded β-hairpins likely share significant structural similarity with the folded β-hairpins observed in the crystal structures of 2AT and KLT (Fig. 2 *A* and *F*).

We turned to native mass spectrometry to further investigate the assembly of 2AT and KLT. Native mass spectrometry has emerged as a powerful tool for studying protein and peptide complexes in the gas phase while preserving noncovalent interactions (100, 101). For these studies, we used an ultra-high mass range (UHMR) Orbitrap mass spectrometer and an ion mobility–mass spectrometry (IM-MS) instrument. In both instruments, 2AT and KLT solutions were introduced using nondisrupting nano-electrospray ionization (102, 103, 104). In UHMR, the high resolution and sensitivity of the orbitrap allow identification of multiple oligomers with multiple charge states. In cIMS, the gas-phase oligomers are separated by size, shape, and charge by applying a traveling wave electric field that carries the oligomers through a cyclic ion mobility cell (105). In both UHMR and cIMS, 2AT and KLT are prepared in a nondenaturing electrolyte solution compatible with mass spectrometry (200 mM ammonium acetate solution at pH 7.4).

The UHMR results show that both 2AT and KLT exhibit different assembly characteristics under the conditions of this experiment. Assemblies of 2AT containing two, three, or four copies of the trimer (hexamers, nonamers, and dodecamers) are the predominant species observed in UHMR-MS, with minor species containing up to ten copies of the trimer also observed (Fig. 4*A*). In contrast, the predominant KLT species observed in UHMR-MS is unassembled trimer, with a minor assembly containing four copies of the trimer also observed (Fig. 4*B*). cIMS of 2AT and KLT shows that the two trimers exhibit similar assembly characteristics under the conditions of this experiment. The IM-MS mobiligrams for both 2AT and KLT show the unassembled trimers as well as assemblies containing two copies of the trimers (Fig. 4 *C* and *D*).

To gain additional insights into the solution-phase assembly of 2AT and KLT, we also used mass photometry. In mass photometry, the contrast of light (reflection and scattering) from individual oligomers in solution is used to measure oligomer sizes and obtain a size distribution (106). Molecular weights of the oligomers are estimated using protein standards analyzed on the mass
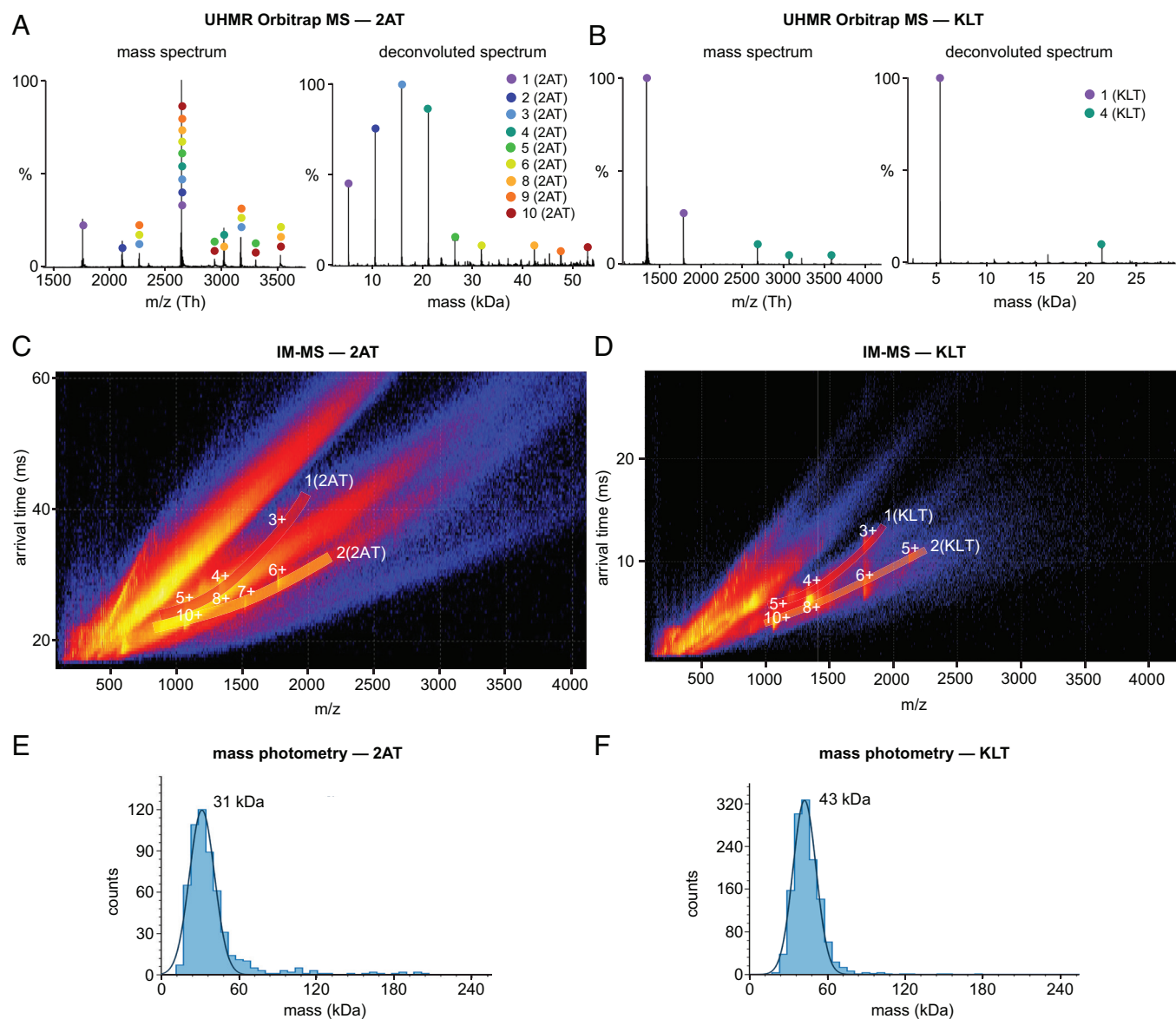
Fig. 4. Mass spectrometric studies of 2AT and KLT. (*A* and *B*) Native mass spectra and deconvolved spectra of 2AT (*A*) and KLT (*B*). Samples were prepared at 40 μM in 200 mM ammonium acetate solution (pH 7.4) and analyzed immediately. (*C* and *D*) Native IM-MS mobilograms of 2AT (*C*) and KLT (*D*). Samples were prepared at 40 μM in 200 mM ammonium acetate solution (pH 7.4) and incubated for 6 h at room temperature and then analyzed. Numeric labels indicate the charge state of the corresponding oligomeric species. (*E* and *F*) Mass photometry analysis of 2AT (*E*) and KLT (*F*). Samples were prepared at 0.65 μM in 200 mM ammonium acetate solution (pH 7.4) and analyzed immediately.

photometry instrument. Mass photometry allows measurement of masses from 30 kDa to 5 MDa and is thus not sensitive to smaller species such as the 5.3 kDa trimers, 10.6 kDa hexamers, 15.9 kDa nonamers, and 21.2 kDa dodecamers. Mass photometry analysis of 2AT and KLT shows that both trimers assemble to form higher-order oligomers containing 6 to 8 copies of the trimer, with the predominant 2AT assembly observed having a molecular weight centered around 31 kDa and the predominant KLT assembly observed having a molecular weight centered around 43 kDa (Fig. 4 *E* and *F*).

The experiments described in the preceding paragraphs demonstrate that 2AT and KLT exhibit markedly different assembly characteristics in solution. 2AT forms a mixture of small soluble oligomers containing 2 to 8 copies of the trimer, while KLT generally forms large aggregates containing more than 50 copies of the trimer with molecular weights greater than 250 kDa. Furthermore, the solution-phase assemblies observed for both 2AT and KLT vary among the different biophysical techniques. While

we do not fully understand what leads to the different assembly characteristics for 2AT and KLT, the assemblies observed for each trimer appear to depend on the conditions under which the experiment is performed as well as the biophysical technique used to observe the assemblies. In X-ray crystallography, cIMS, and mass photometry, 2AT and KLT exhibit similar assembly properties. However, 2AT and KLT exhibit contrasting assembly behaviors in SDS-PAGE and UHMR, suggesting that structural differences between the two trimers impact solution-phase assembly under the conditions of these techniques. Table 1 summarizes the structural and biophysical data for 2AT and KLT and highlights the multifarious assembly characteristics of the two trimers.

Cell-Based Biological Studies of 2AT and KLT. Exposing cells in culture to oligomers of full-length Aβ elicits a multitude of downstream cellular events that culminate in cell toxicity and cell death (*SI Appendix*, Fig. S8) (17, 20, 107). We sought to determine whether 2AT and KLT also exhibit toxicity toward

Table 1. Oligomer sizes observed for 2AT and KLT in the structural and biophysical studies

Trimer	X-ray crystallography	SDS-PAGE	UHMR	cIMS	Mass photometry
2AT	4	1, 2, 3, 4, and larger	1, 2, 3, 4, and larger	1 and 2	6–8
KLT	4	1–2 and >50	1 and 4	1 and 2	6–8

cells and whether the differences in structure and solution-phase assembly between 2AT and KLT lead to differences in cellular toxicity. To investigate the toxicity of 2AT and KLT, we examined three toxicity markers—changes in ATP levels, cell viability, and activation of the apoptosis marker caspase-3/7—in SH-SY5Y cells exposed to 2AT or KLT. SH-SY5Y cells are a human neuroblastoma cell line commonly used in cell-based studies of Aβ oligomers (108, 109). For all three toxicity assays, we exposed the cells to varying concentrations of 2AT or KLT (50 to 0.2 μM) (110, 111, 112) or deionized water (vehicle) for 72 h and then performed the assays according to the manufacturer's instructions.

The cell-based assays indicate that 2AT and KLT both exhibit toxicity toward SH-SY5Y cells, with 2AT showing greater toxicity than KLT. The assays also indicate that 2AT and KLT may elicit toxicity through different mechanisms. 2AT and KLT both induce a reduction in ATP levels at concentrations as low as 1.6 μM, but at concentrations above 12.5 μM, 2AT induces a twofold greater reduction in ATP levels (Fig. 5A). 2AT and KLT both reduce cell viability at concentrations as low as 12.5 μM, with 2AT exhibiting a greater effect on cell viability at concentrations above 12.5 μM (Fig. 5B). 2AT induces activation of caspase-3/7, eliciting an increase in caspase-3/7 activity at concentrations as low as 6.3 μM (Fig. 5C). In contrast, KLT induces little or no increase in caspase-3/7 activity at any of the concentrations tested. The cytotoxicity data suggest that 2AT elicits toxicity by activating apoptosis, which leads to a decrease in ATP levels and cell viability, whereas KLT does not appear to activate apoptosis, instead eliciting a decrease in ATP levels and cell viability through an alternative mechanism.

To further investigate the biological properties of 2AT and KLT, and to gain insights into why the two trimers appear to elicit toxicity through different mechanisms, we visualized how each trimer interacts with SH-SY5Y cells using fluorescence microscopy. We prepared analogues of 2AT and KLT singly labeled with the fluorophore sulfo-cyanine3 (2AT-sCy3 and KLT-sCy3) and then used live-cell fluorescence microscopy to visualize SH-SY5Y cells exposed to the labeled trimers. We have previously found that single labeling with sCy3 of a related triangular timer marginally impacts the assembly properties of the trimer (113). The microscopy studies reveal that 2AT-sCy3 and KLT-sCy3 interact with the cells differently. 2AT-sCy3 accumulates as punctate features inside the cells (Fig. 5D), whereas KLT-sCy3 does not appear to significantly enter the cells and instead accumulates as punctate features on the plasma membrane (Fig. 5F).

The punctate appearance and intracellular localization of 2AT-sCy3 suggest that 2AT-sCy3 enters the cells through an endocytic mechanism. To investigate whether 2AT-sCy3 enters the cells through endocytosis, we concurrently treated cells with 2AT-sCy3 and the fluorescent dye LysoTracker™ (ThermoFisher Scientific), which stains acidic late endosomes and lysosomes. Live-cell fluorescence microscopy of these cells reveals that 2AT-sCy3 colocalizes with LysoTracker, providing evidence that 2AT enters the cells

through endocytosis (Fig. 5E). In contrast, live-cell fluorescence microscopy of cells treated KLT-sCy3 and LysoTracker reveals that KLT-sCy3 does not colocalize with LysoTracker (Fig. 5G).

The different ways that 2AT-sCy3 and KLT-sCy3 interact with SH-SY5Y cells are consistent with how different assemblies of full-length Aβ have been reported to interact with cells. 2AT appears to enter the cells through endocytic uptake and accumulates in intracellular endosomes. Endocytic uptake and intracellular accumulation of Aβ is an established pathway by which Aβ enters cells and forms aggregates (114, 115, 116), and some evidence suggests that intracellular accumulation of Aβ precedes plaque formation (117, 118, 119). KLT appears to accumulate on the cell membrane without significantly entering the cells. Some Aβ oligomers directly interact with the cell membrane and do not enter cells, instead accumulating on the membrane as punctate high-molecular-weight aggregates (120, 121).

Although we do not fully understand what leads to the differences in toxicity and cellular interactions between 2AT and KLT, we believe that these differences may arise from the structural and assembly differences between the two trimers. In the membrane-like environment of SDS-PAGE, 2AT forms smaller oligomers, whereas KLT forms higher-molecular-weight aggregates. These differences in assembly may help explain why 2AT-sCy3 appears to enter the cells through an endocytic pathway and KLT-sCy3 appears to aggregate on the exterior of the cells. The endocytic uptake of 2AT may also lead to activation of caspase-3/7-mediated apoptosis by 2AT.

Effects of 2AT and KLT on Aβ$_{42}$. To better understand the relationship between the Aβ oligomer models 2AT and KLT and full-length Aβ, we studied the effects of 2AT and KLT on Aβ$_{42}$ fibrillization, Aβ$_{42}$ toxicity, and Aβ$_{42}$ cellular interaction. In these studies, we found that 2AT and KLT affect Aβ$_{42}$ differently, with KLT showing a greater effect in each experiment.

To investigate the effect of 2AT and KLT on Aβ$_{42}$ fibrillization, we performed thioflavin T (ThT) aggregation assays on 5 μM Aβ$_{42}$ in the presence of varying concentrations of 2AT or KLT. In the ThT assays, KLT dramatically impacts Aβ$_{42}$ fibrilization, completely suppressing fibrilization after 5 h at concentrations as low 0.625 μM (Fig. 6B and *SI Appendix*, Fig. S7C). At concentrations less than 0.625 μM, KLT increases the lag time of fibrilization and decreases end-point ThT fluorescence intensity in a dose-dependent manner. Even concentrations of KLT as low as 0.078 μM (0.016 molar equivalents) significantly increase the lag time. In contrast, concentrations of 2AT up to 1.25 μM have little or no effect on the lag time of fibrilization but moderately decrease end-point ThT fluorescence intensity (Fig. 6A and *SI Appendix*, Figs. S5A and S7B). These findings indicate that KLT interacts with full-length Aβ$_{42}$ to a much greater extent than 2AT.

To investigate the effect of 2AT and KLT on Aβ$_{42}$ toxicity, we performed a series of cell-based toxicity experiments in which we examined four toxicity markers—LDH release, changes in ATP levels, caspase-3/7 activation, and cell viability—in SH-SY5Y cells exposed to Aβ$_{42}$ in the absence or presence of 2AT and KLT. We first identified an Aβ$_{42}$ concentration that elicits significant toxicity in the absence of 2AT and KLT by exposing SH-SY5Y cells to varying concentrations of Aβ$_{42}$ and then performing the toxicity assays. The toxicity markers establish that Aβ$_{42}$ elicits significant toxicity at 6 μM (*SI Appendix*, Fig. S8). We next investigated the effect of 2AT and KLT on Aβ$_{42}$ toxicity by exposing SH-SY5Y cells to 6 μM Aβ$_{42}$ in the presence of a twofold dilution series of 2AT or KLT (12 to 0.09 μM) and then performing the toxicity assays.

2AT and KLT have opposite effects on Aβ$_{42}$ toxicity. 2AT appears to moderately inhibit Aβ$_{42}$ toxicity at concentrations
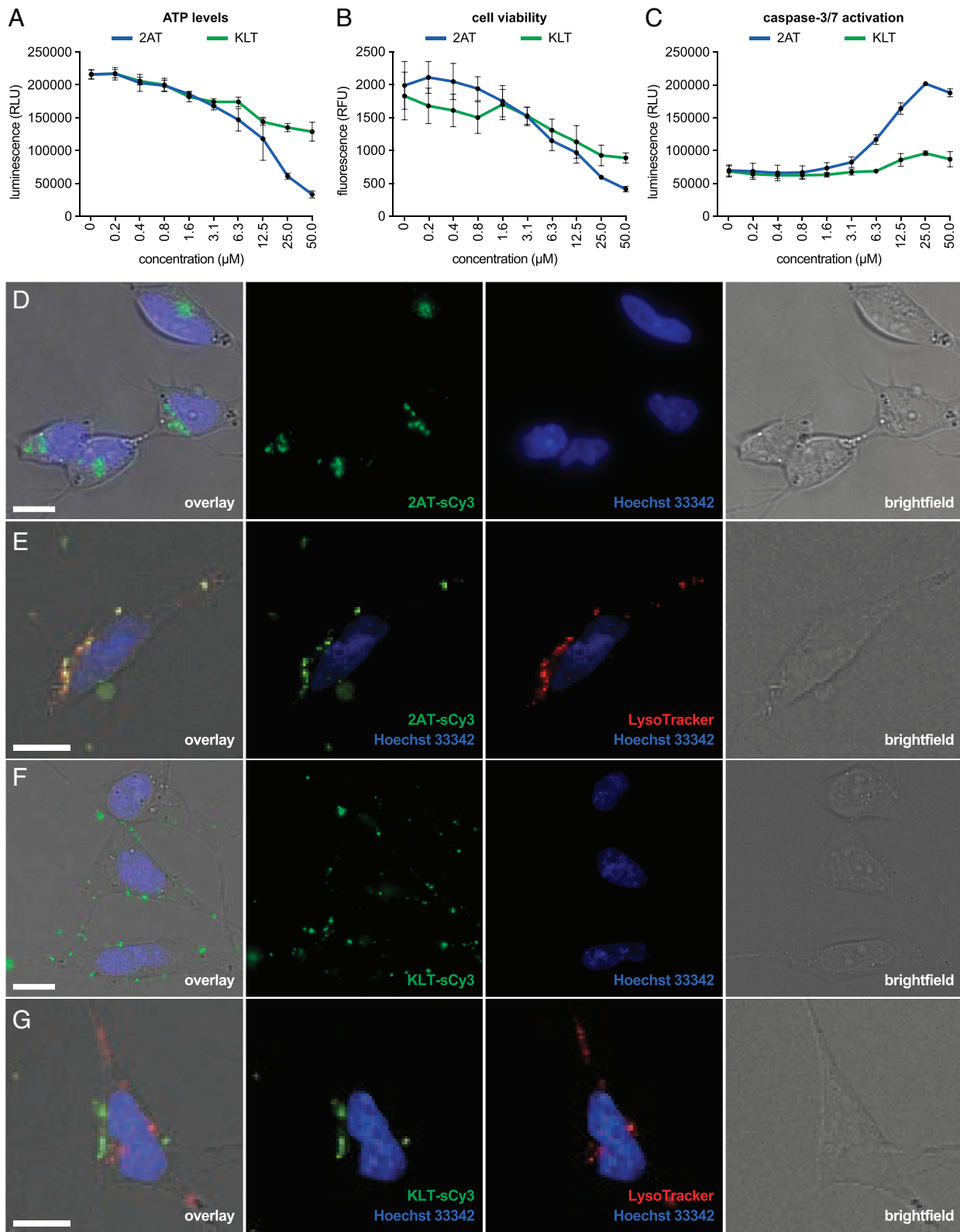
Fig. 5. Cell-based biological studies of 2AT and KLT. (*A*) CellTiter-Glo ATP assay. (*B*) ApoLive-Glo cell viability assay. (*C*) ApoLive-Glo caspase-3/7 activation assay. The cell-based assays in *A–C* were performed by exposing SH-SY5Y cells to a twofold dilution series of 2AT or KLT for 72 h. The cell-based experiments were performed on 2AT and KLT side-by-side on the same plate of cells to ensure identical experimental conditions. All data from the assays are shown as the mean of three technical replicates, with error bars representing the SD. (*D–G*) Representative live-cell fluorescence and brightfield micrographs of SH-SY5Y cells after treatment with 1 μM 2AT-sCy3 (*D*), 1 μM 2AT-sCy3 and LysoTracker (*E*), 1 μM KLT-sCy3 (*F*), or 1 μM KLT-sCy3 and LysoTracker (*G*); (Scale bars, 10 μm).

between 0.75 μM and 3 μM, eliciting a slight decrease in LDH release and caspase-3/7 activation and a slight increase in ATP levels and cell viability at these concentrations relative to 6 μM $A\beta_{42}$ alone (blue traces in Fig. 7 *A–D*). At 2AT concentrations greater than 3 μM, the inhibitory effect is diminished for all four toxicity markers, likely due to the toxic nature of 2AT at these higher concentrations (Fig. 5 *A–C*). In contrast, KLT appears to promote $A\beta_{42}$ toxicity at concentrations greater than 0.75 μM,

A

ThT aggregation assay of 5 µM Aβ₄₂ with varying concentrations of 2AT

- ● 0 µM 2AT
- ● 0.010 µM 2AT
- ● 0.020 µM 2AT
- ● 0.039 µM 2AT
- ● 0.078 µM 2AT
- ● 0.156 µM 2AT
- ● 0.313 µM 2AT
- ● 0.625 µM 2AT
- ● 1.25 µM 2AT

B

ThT aggregation assay of 5 µM Aβ₄₂ with varying concentrations of KLT

- ● 0 µM KLT
- ● 0.010 µM KLT
- ● 0.020 µM KLT
- ● 0.039 µM KLT
- ● 0.078 µM KLT
- ● 0.156 µM KLT
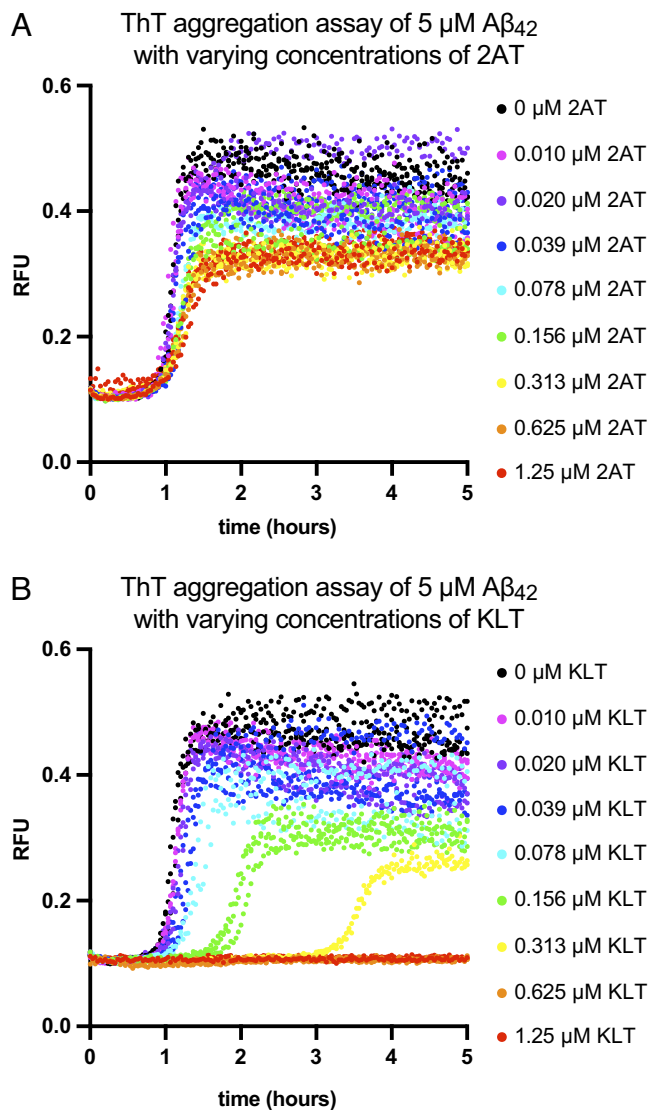- ● 0.313 µM KLT
- ● 0.625 µM KLT
- ● 1.25 µM KLT

Fig. 6. The effects of 2AT and KLT on Aβ₄₂ fibrillization. ThT aggregation assays of 5 µM Aβ₄₂ in the presence of varying concentrations of 2AT (*A*) or KLT (*B*) were performed at 25 °C under quiescent conditions in PBS (10 mM Na_2HPO_4, 1.8 mM KH_2PO_4, 137 mM NaCl, 2.7 mM KCl) at pH 7.4 containing 10 µM ThT. Fluorescence of ThT was monitored at 440 nm excitation and 485 nm emission.

eliciting an increase in LDH release and caspase-3/7 activation and a decrease in ATP levels and cell viability relative to 6 µM Aβ₄₂ alone (green traces in Fig. 7 *A–D*).

To further investigate the effects of 2AT and KLT on Aβ₄₂ cell biology, and to gain insights into why the two trimers exhibit opposite effects on Aβ₄₂ toxicity, we visualized the cellular interactions of fluorescently labeled Aβ₄₂ in the absence and presence of 2AT and KLT. For these experiments, we exposed SH-SY5Y cells to 1 µM solutions of *N*-terminally labeled HiLyte™ Fluor 647-Aβ₄₂ (HL647-Aβ₄₂) containing 0 µM, 2 µM, or 4 µM 2AT or KLT and then used live-cell fluorescence microscopy to visualize and quantify HL647-Aβ₄₂ fluorescence on the cells. In the absence of 2AT and KLT, HL647-Aβ₄₂ accumulates as punctate features inside the cells (Fig. 7*E*), which is consistent with previous observations (116).

2AT and KLT appear to have opposite effects on the cellular interactions of Aβ₄₂. In the presence of 2AT, HL647-Aβ₄₂ exhibits reduced accumulation in the cells (Fig. 7 *F* and *G*), whereas in the presence of KLT, HL647-Aβ₄₂ exhibits increased accumulation in and on the cells (Fig. 7 *H* and *I*). Quantification of the total

fluorescence intensity from HL647-Aβ₄₂ indicates that in the presence of 2 µM and 4 µM 2AT, there is approximately a twofold to threefold reduction in cellular HL647-Aβ₄₂. In contrast, in the presence of 2 µM and 4 µM KLT, there is approximately a 1.5- to 14-fold increase in cellular HL647-Aβ₄₂.

These fluorescence microscopy experiments shed light on why 2AT inhibits Aβ₄₂ toxicity and KLT promotes Aβ₄₂ toxicity. 2AT appears to inhibit the interaction of Aβ₄₂ with cells and thus reduces the toxicity of Aβ₄₂ toward the cells; KLT appears to promote the interaction of Aβ₄₂ with cells and thus increases the toxicity of Aβ₄₂ toward the cells. Although we do not yet understand why 2AT and KLT affect the cellular interaction and toxicity of Aβ₄₂ differently, we speculate that 2AT may prevent Aβ₄₂ toxicity by binding and sequestering Aβ₄₂ monomers or oligomers, whereas KLT may promote Aβ₄₂ toxicity by interacting with the cell membranes and recruiting Aβ₄₂ to the cell membranes.

Summary and Conclusion

The structural, biophysical, and biological studies of 2AT and KLT provide evidence that both trimers share biophysical and biological characteristics with oligomers of full-length Aβ, which thus suggests that 2AT and KLT are suitable models for Aβ oligomers. In X-ray crystallography, 2AT and KLT assemble to form dodecamers in the crystal lattice. In the variety of conditions used for the biophysical studies, 2AT forms small soluble oligomers ranging from hexamers, nonamers, and dodecamers and larger, and KLT forms high-molecular-weight aggregates. Aβ oligomers of these sizes have been observed in protein extracts from mouse and human brains and are thought to be important in Alzheimer's disease (17, 19, 20).

Recently, the identification, characterization, and study of the putative Aβ dodecamer Aβ*56 has been called into question (27, 28). While we do not know whether Aβ*56 is real or an artifact, the formation of crystallographic dodecamers by the constrained Aβ β-hairpin peptides 2AM and KLM demonstrates that peptides derived from Aβ have a propensity to form dodecamers. The further observation that the covalently linked trimers 2AT and KLT are easy to prepare from monomers and both form crystallographic dodecamers (Fig. 2) and that 2AT forms dodecamers in SDS-PAGE (Fig. 3*A*) lends further credence to the idea that dodecamers are inherently stable structures.

Like oligomers of full-length Aβ, trimers 2AT and KLT are toxic toward cells in culture. The toxicity studies suggest that both trimers elicit toxicity by interacting with the cells and decreasing cell viability and ATP levels. The activation of caspase-3/7-mediated apoptosis by only 2AT suggests that 2AT interacts with and affects cells differently than KLT. The variation in apoptosis activation between 2AT and KLT demonstrates that different Aβ oligomer models have different biological properties, which may help explain why different oligomers of full-length Aβ exhibit different biological properties. In further support that 2AT and KLT elicit toxicity through different mechanisms, fluorescence microscopy demonstrates that the two trimers interact with cells differently. The differing cellular interactions of 2AT and KLT may help explain why some Aβ oligomers enter cells and other higher-molecular-weight oligomers accumulate on cell membranes.

The effects of 2AT and KLT on Aβ₄₂ aggregation, toxicity, and cellular interaction establish that the trimers interact with full-length Aβ₄₂. KLT appears to more readily interact with Aβ₄₂, considerably inhibiting Aβ₄₂ fibrillization at substoichiometric concentrations and promoting Aβ₄₂ toxicity and cell interactions. In contrast, 2AT appears to interact less strongly with Aβ₄₂, exhibiting a moderate effect on Aβ₄₂ fibrillization and a modest inhibitory effect on Aβ₄₂ toxicity and cell interactions. These different
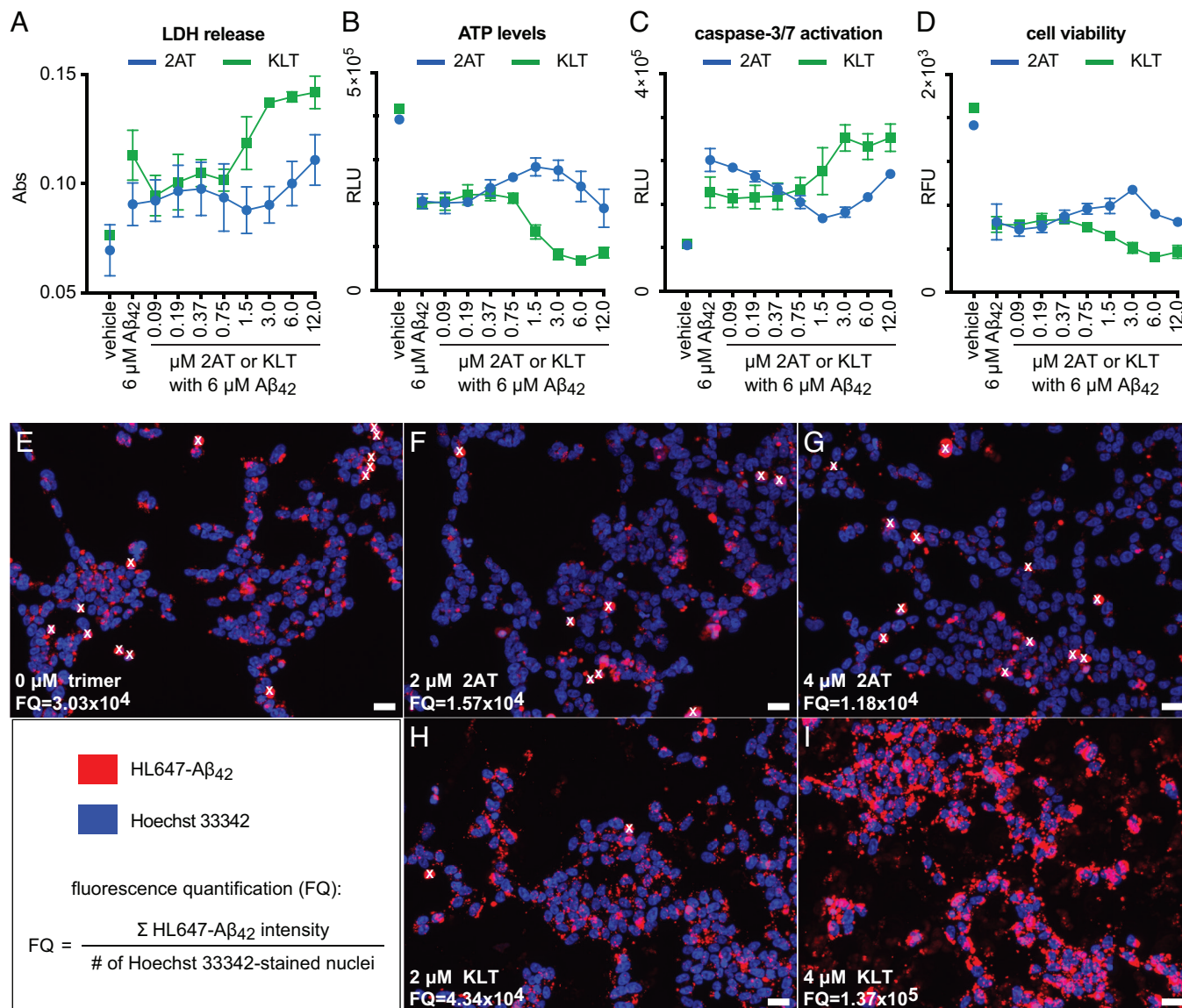
Fig. 7. The effects of 2AT and KLT on Aβ$_{42}$ toxicity and cellular interaction (*A–D*). (*A*) LDH release assay (*B*) CellTiter-Glo ATP assay. (*C*) ApoLive-Glo cell viability assay. (*D*) ApoLive-Glo caspase-3/7 activation assay. The cell-based assays in *A–D* were performed by exposing SH-SY5Y cells to 6 µM Aβ$_{42}$ in the presence of a twofold dilution series of 2AT and KLT for 72 h. All data from the assays are shown as the mean of three technical replicates, with error bars representing the SD. (*E–I*) Live-cell fluorescence micrographs of SH-SY5Y cells after treatment with 1 µM HiLyte™ Fluor 647-Aβ$_{42}$ (HL647-Aβ$_{42}$) in the presence of 0 µM trimer (*E*) or 2 µM and 4 µM 2AT (*F* and *G*) or 2 µM and 4 µM KLT (*H* and *I*) for 16 h; (Scale bars, 20 µm.) Fluorescence quantification (FQ), as determined by (total fluorescence of HL647Aβ$_{42}$)/(total number of cells) is indicated on each micrograph. Dead cells were excluded from the fluorescence quantification analysis and are marked with a white "x".

behaviors likely arise from the different structural and assembly properties of 2AT and KLT. These findings suggest a model in which oligomers of full-length Aβ composed of β-hairpins with different β-strand alignments differentially impact the aggregation, toxicity, and cellular interaction of other Aβ species.

Aβ oligomers that are prepared in vitro or isolated from tissue consist of a variety of different sizes and exhibit varying toxicities (17, 19, 20). The assembly and toxicity characteristics that researchers observe for a particular Aβ oligomer or mixture of Aβ oligomers appear to depend on the conditions under which the oligomers are prepared or isolated (20). The dizzying array of techniques reported for Aβ oligomer preparation and isolation has painted a complex picture of Aβ oligomers and has led to conflicting results and viewpoints about the significance of Aβ oligomers in Alzheimer's disease. The varying assembly and biological characteristics exhibited by 2AT and KLT may help shed light on

the disparate behaviors exhibited by different preparations or isolations of Aβ oligomers.

The study of 2AT and KLT support a model for the assembly of full-length Aβ in which Aβ folds to form β-hairpins with different β-strand alignments, which in turn assemble to form different sizes of oligomers with different biological properties. Some β-strand alignments lead to lower-molecular-weight oligomers that enter the cells and activate caspase-3/7-mediated apoptosis, which leads to a reduction in ATP levels and cell viability and eventual cell death. Other β-strand alignments lead to higher molecular weight aggregates that accumulate on the plasma membrane, which leads to an apoptosis-independent reduction in ATP levels and cell viability and eventual cell death. We recognize that our peptides and oligomers are chemical models and should thus be interpreted cautiously. While we do not yet know whether our trimer and dodecamer structures

mimic the actual structures of Aβ oligomers formed in vitro or in the brain, we are actively attempting to address this question in our laboratory.

Materials and Methods

Detailed methods are provided in the Supporting Information. KLM$_{CC}$ was synthesized using standard Fmoc-based solid-phase peptide synthesis. KLT was synthesized by oxidizing KLM$_{CC}$ in 20% aqueous DMSO for 48 hours. X-ray diffraction data for KLT and KLT$_I$ were collected on a Rigaku Micromax-007HF X-ray diffractometer with a rotating copper anode, and the X-ray crystallographic phases were determined using molecular replacement and SAD phasing. SDS-PAGE was performed using 16.5% Mini-PROTEAN® Tris-Tricine Gels and an 8 to 16% Mini-PROTEAN® TGX Stain-Free Protein Gels. Silver staining was performed as previously described (122). CD spectroscopy was performed on a Jasco J-810 CD spectropolarimeter. UHMR-MS, IM-MS, and mass photometry were performed on a Thermo Q Exactive UHMR Orbitrap MS, Waters SELECT SERIES Cyclic Ion Mobility Spectrometry Q-cIMS-TOF system, and a TwoMP mass photometer. Cellular toxicity assays were performed on SH-SY5Y cells using the CyQUANT™ LDH Cytotoxicity Assay, the CellTiter-Glo® 2.0 Cell Viability Assay, and the ApoLive-Glo™ Multiplex Assay. 2AT and KLT were labeled with sulfo-cyanine3 by treating the trimers with sulfo-cyanine3 NHS ester. Live-cell fluorescence microscopy was performed on SH-SY5Y cells adhered to an Ibidi μ-Slide eight Well Chamber Slide. The cells were imaged using a Keyence BZ-X810 fluorescence microscope and analyzed using the Hybrid Cell Count application in the BZ-X810 Analyzer software. ThT assays were performed on 5 μM Aβ$_{42}$ in PBS at pH 7.4 containing 10 μM ThT in the presence of a dilution series of 2AT or KLT (10 to 0.01 μM, 0 μM) in Corning® 96-well Half Area Black/Clear Flat Bottom Polystyrene NBS Microplates.

Author affiliations: [a]Department of Chemistry, University of California Irvine, Irvine, CA 92697; [b]Department of Pharmaceutical Sciences, University of California Irvine, Irvine, CA 92697; [c]Department of Biochemistry, Albert Einstein College of Medicine, Bronx, NY 10461; and [d]Resource for Native Mass Spectrometry Guided Structural Biology, The Ohio State University, Columbus, OH 43210

1. M. P. Lambert et al., Diffusible, nonfibrillar ligands derived from Abeta1-42 are potent central nervous system neurotoxins. Proc. Natl. Acad. Sci. U.S.A. **95**, 6448–6453 (1998).
2. M. Enya et al., Appearance of sodium dodecyl sulfate-stable amyloid beta-protein (Abeta) dimer in the cortex during aging. Am. J. Pathol. **154**, 271–279 (1999).
3. D. J. Selkoe, Alzheimer's disease is a synaptic failure. Science **298**, 789–791 (2002).
4. R. G. Nagele, M. R. D'Andrea, W. J. Anderson, H.-Y. Wang, Intracellular accumulation of beta-amyloid(1-42) in neurons is facilitated by the alpha 7 nicotinic acetylcholine receptor in Alzheimer's disease. Neuroscience **110**, 199–211 (2002).
5. D. M. Walsh et al., Naturally secreted oligomers of amyloid beta protein potently inhibit hippocampal long-term potentiation in vivo. Nature **416**, 535–539 (2002).
6. M. Townsend, G. M. Shankar, T. Mehta, D. M. Walsh, D. J. Selkoe, Effects of secreted oligomers of amyloid beta-protein on hippocampal synaptic plasticity: A potent role for trimers. J. Physiol. **572**, 477–492 (2006).
7. C. Haass, D. J. Selkoe, Soluble protein oligomers in neurodegeneration: lessons from the Alzheimer's amyloid beta-peptide. Nat. Rev. Mol. Cell Biol. **8**, 101–112 (2007).
8. G. M. Shankar et al., Amyloid-beta protein dimers isolated directly from Alzheimer's brains impair synaptic plasticity and memory. Nat. Med. **14**, 837–842 (2008).
9. W.-Q. Zhao et al., Amyloid beta oligomers induce impairment of neuronal insulin receptors. FASEB J. **22**, 246–260 (2008).
10. H. W. Querfurth, F. M. LaFerla, Alzheimer's disease. N. Engl. J. Med. **362**, 329–344 (2010).
11. M. Fändrich, Oligomeric intermediates in amyloid formation: structure determination and mechanisms of toxicity. J. Mol. Biol. **421**, 427–440 (2012).
12. E. K. Pickett et al., Non-fibrillar oligomeric Amyloid-β within synapses. J. Alzheimers. Dis. **53**, 787–800 (2016).
13. Z. Wang et al., Human brain-derived Aβ oligomers bind to synapses and disrupt synaptic activity in a manner that requires APP. J. Neurosci. **37**, 11947–11966 (2017).
14. W. Hong et al., Diffusible, highly bioactive oligomers represent a critical minority of soluble Aβ in Alzheimer's disease brain. Acta Neuropathol. **136**, 19–40 (2018).
15. R. Nortley et al., Amyloid β oligomers constrict human capillaries in Alzheimer's disease via signaling to pericytes. Science **365**, eaav9518 (2019).
16. B. Zott et al., A vicious cycle of β amyloid-dependent neuronal hyperactivation. Science **365**, 559–565 (2019).
17. E. N. Cline, M. A. Bicca, K. L. Viola, W. L. Klein, The Amyloid-β oligomer hypothesis: Beginning of the third decade. J. Alzheimers. Dis. **64**, S567–S610 (2018).
18. K. H. Ashe, The biogenesis and biology of amyloid β oligomers in the brain. Alzheimers. Dement. **16**, 1561–1567 (2020).
19. M. E. Larson, S. E. Lesné, Soluble Aβ oligomer production and toxicity. J. Neurochem. **120**, 125–139 (2012).
20. I. Benilova, E. Karran, B. De Strooper, The toxic Aβ oligomer and Alzheimer's disease: An emperor in need of clothes. Nat. Neurosci. **15**, 349–357 (2012).
21. G. Brinkmalm et al., Identification of neurotoxic cross-linked amyloid-β dimers in the Alzheimer's brain. Brain **142**, 1441–1457 (2019).
22. T. Yang, S. Li, H. Xu, D. M. Walsh, D. J. Selkoe, Large soluble oligomers of Amyloid β-protein from alzheimer brain are far less neuroactive than the smaller oligomers to which they dissociate. J. Neurosci. **37**, 152–163 (2017).
23. M. Handoko et al., Correlation of specific amyloid-β oligomers with tau in cerebrospinal fluid from cognitively normal older adults. JAMA Neurol. **70**, 594–599 (2013).
24. S. Lesné et al., A specific amyloid-beta protein assembly in the brain impairs memory. Nature **440**, 352–357 (2006).
25. P. Liu et al., Quaternary structure defines a large class of Amyloid-β oligomers neutralized by sequestration. Cell Rep. **11**, 1760–1771 (2015).
26. S. E. Lesné et al., Brain amyloid-β oligomers in ageing and Alzheimer's disease. Brain **136**, 1383–1398 (2013).
27. C. Piller, Blots on a field? Science **377**, 358–363 (2022).
28. K. H. Ashe, Alzheimer's target still viable but untested. Science **377**, 935 (2022).
29. F. Amar et al., The amyloid-β oligomer Aβ*56 induces specific alterations in neuronal signaling that lead to tau phosphorylation and aggregation. Sci. Signal. **10**, eaal2021 (2017).
30. M. A. Sherman et al., Soluble conformers of Aβ and Tau alter selective proteins governing axonal transport. J. Neurosci. **36**, 9647–9658 (2016).
31. M. Jin et al., Soluble amyloid beta-protein dimers isolated from Alzheimer cortex directly induce Tau hyperphosphorylation and neuritic degeneration. Proc. Natl. Acad. Sci. U.S.A. **108**, 5819–5824 (2011).
32. A. K. Paravastu, R. D. Leapman, W.-M. Yau, R. Tycko, Molecular structural basis for polymorphism in Alzheimer's beta-amyloid fibrils. Proc. Natl. Acad. Sci. U.S.A. **105**, 18349–18354 (2008).
33. A. T. Petkova, W.-M. Yau, R. Tycko, Experimental constraints on quaternary structure in Alzheimer's beta-amyloid fibrils. Biochemistry **45**, 498–512 (2006).
34. J.-X. Lu et al., Molecular structure of β-amyloid fibrils in Alzheimer's disease brain tissue. Cell **154**, 1257–1268 (2013).
35. W. Qiang, W.-M. Yau, Y. Luo, M. P. Mattson, R. Tycko, Antiparallel β-sheet architecture in Iowa-mutant β-amyloid fibrils. Proc. Natl. Acad. Sci. U.S.A. **109**, 4443–4448 (2012).
36. M. A. Wälti et al., Atomic-resolution structure of a disease-relevant Aβ(1–42) amyloid fibril. Proc. Natl. Acad. Sci. U.S.A. **113**, E4976–84 (2016).
37. M. T. Colvin et al., Atomic resolution structure of monomorphic Aβ42 amyloid fibrils. J. Am. Chem. Soc. **138**, 9663–9674 (2016).
38. Y. Xiao et al., Aβ(1–42) fibril structure illuminates self-recognition and replication of amyloid in Alzheimer's disease. Nat. Struct. Mol. Biol. **22**, 499–505 (2015).
39. L. Gremer et al., Fibril structure of amyloid-β(1–42) by cryo-electron microscopy. Science **358**, 116–119 (2017).
40. Y. Yang et al., Cryo-EM structures of amyloid-β 42 filaments from human brains. Science **375**, 167–172 (2022).
41. M. D. Tuttle et al., Solid-state NMR structure of a pathogenic fibril of full-length human α-synuclein. Nat. Struct. Mol. Biol. **23**, 409–415 (2016).
42. A. W. P. Fitzpatrick et al., Cryo-EM structures of tau filaments from Alzheimer's disease. Nature **547**, 185–190 (2017).
43. A. J. Dregni et al., In vitro 0N4R tau fibrils contain a monomorphic β-sheet core enclosed by dynamically heterogeneous fuzzy coat segments. Proc. Natl. Acad. Sci. U.S.A. **116**, 16357–16366 (2019).
44. B. Falcon et al., Structures of filaments from Pick's disease reveal a novel tau protein fold. Nature **561**, 137–140 (2018).
45. M. Kollmer et al., Cryo-EM structure and polymorphism of Aβ amyloid fibrils purified from Alzheimer's brain tissue. Nat. Commun. **10**, 4760 (2019).
46. C. Glynn et al., Cryo-EM structure of a human prion fibril with a hydrophobic, protease-resistant core. Nat. Struct. Mol. Biol. **27**, 417–423 (2020).
47. M. Schweighauser et al., Structures of α-synuclein filaments from multiple system atrophy. Nature **585**, 464–469 (2020).
48. C. Röder et al., Cryo-EM structure of islet amyloid polypeptide fibrils reveals similarities with amyloid-β fibrils. Nat. Struct. Mol. Biol. **27**, 660–667 (2020).
49. R. Kayed et al., Common structure of soluble amyloid oligomers implies common mechanism of pathogenesis. Science **300**, 486–489 (2003).
50. D. Burdick et al., Assembly and aggregation properties of synthetic Alzheimer's A4/beta amyloid peptide analogs. J. Biol. Chem. **267**, 546–554 (1992).
51. B. Soreghan, J. Kosmoski, C. Glabe, Surfactant properties of Alzheimer's A beta peptides and the mechanism of amyloid aggregation. J. Biol. Chem. **269**, 28551–28554 (1994).
52. D. M. Walsh, A. Lomakin, G. B. Benedek, M. M. Condron, D. B. Teplow, Amyloid beta-protein fibrillogenesis. Detection of a protofibrillar intermediate. J. Biol. Chem. **272**, 22364–22372 (1997).

53. J. D. Harper, S. S. Wong, C. M. Lieber, P. T. Lansbury, Observation of metastable Abeta amyloid protofibrils by atomic force microscopy. *Chem. Biol.* **4**, 119–125 (1997).
54. C. A. Lasagna-Reeves, C. G. Glabe, R. Kayed, Amyloid-β annular protofibrils evade fibrillar fate in Alzheimer disease brain. *J. Biol. Chem.* **286**, 22122–22130 (2011).
55. H. Kokubo et al., Amyloid Beta annular protofibrils in cell processes and synapses accumulate with aging and Alzheimer-associated genetic modification. *Int. J. Alzheimers. Dis.* **2009**, 689285 (2009).
56. R. Kayed et al., Annular protofibrils are a structurally and functionally distinct type of amyloid oligomer. *J. Biol. Chem.* **284**, 4230–4237 (2009).
57. S. Barghorn et al., Globular amyloid beta-peptide oligomer - A homogenous and stable neuropathological protein in Alzheimer's disease. *J. Neurochem.* **95**, 834–847 (2005).
58. M. Hoshi et al., Spherical aggregates of beta-amyloid (amylospheroid) show high neurotoxicity and activate tau protein kinase I/glycogen synthase kinase-3beta. *Proc. Natl. Acad. Sci. U.S.A.* **100**, 6370–6375 (2003).
59. W. B. Stine Jr., K. N. Dahlgren, G. A. Krafft, M. J. LaDu, In vitro characterization of conditions for amyloid-beta peptide oligomerization and fibrillogenesis. *J. Biol. Chem.* **278**, 11612–11622 (2003).
60. D. M. Walsh, I. Klyubin, J. V. Fadeeva, M. J. Rowan, D. J. Selkoe, Amyloid-beta oligomers: their production, toxicity and therapeutic inhibition. *Biochem. Soc. Trans.* **30**, 552–557 (2002).
61. N. J. Economou et al., Amyloid β-protein assembly and Alzheimer's disease: Dodecamers of Aβ42, but not of Aβ40, seed fibril formation. *J. Am. Chem. Soc.* **138**, 1772–1775 (2016).
62. S. L. Bernstein et al., Amyloid-β protein oligomerization and the importance of tetramers and dodecamers in the aetiology of Alzheimer's disease. *Nat. Chem.* **1**, 326–331 (2009).
63. G. Bitan, A. Lomakin, D. B. Teplow, Amyloid beta-protein oligomerization: Prenucleation interactions revealed by photo-induced cross-linking of unmodified proteins. *J. Biol. Chem.* **276**, 35176–35184 (2001).
64. G. Bitan et al., Amyloid beta -protein (Abeta) assembly: Abeta 40 and Abeta 42 oligomerize through distinct pathways. *Proc. Natl. Acad. Sci. U.S.A.* **100**, 330–335 (2003).
65. G. Bitan, S. S. Vollers, D. B. Teplow, Elucidation of primary structure elements controlling early amyloid beta-protein oligomerization. *J. Biol. Chem.* **278**, 34882–34889 (2003).
66. K. Ono, M. M. Condron, D. B. Teplow, Structure-neurotoxicity relationships of amyloid beta-protein oligomers. *Proc. Natl. Acad. Sci. U.S.A.* **106**, 14745–14750 (2009).
67. B. O'Nuallain et al., Amyloid beta-protein dimers rapidly form stable synaptotoxic protofibrils. *J. Neurosci.* **30**, 14411–14419 (2010).
68. T. T. O'Malley et al., Aβ dimers differ from monomers in structural propensity, aggregation paths and population of synaptotoxic assemblies. *Biochem. J.* **461**, 413–426 (2014).
69. F. Hasecke et al., Origin of metastable oligomers and their effects on amyloid fibril self-assembly. *Chem. Sci.* **9**, 5937–5948 (2018).
70. A. Laganowsky et al., Atomic view of a toxic amyloid small oligomer. *Science* **335**, 1228–1231 (2012).
71. S. Sangwan et al., Atomic structure of a toxic, oligomeric segment of SOD1 linked to amyotrophic lateral sclerosis (ALS). *Proc. Natl. Acad. Sci. U.S.A.* **114**, 8770–8775 (2017).
72. M. I. Apostol, K. Perry, W. K. Surewicz, Crystal structure of a human prion protein fragment reveals a motif for oligomer formation. *J. Am. Chem. Soc.* **135**, 10202–10205 (2013).
73. V. A. Streltsov, J. N. Varghese, C. L. Masters, S. D. Nuttall, Crystal structure of the amyloid-β p3 fragment provides a model for oligomer formation in Alzheimer's disease. *J. Neurosci.* **31**, 1419–1426 (2011).
74. S. Chimon et al., Evidence of fibril-like β-sheet structures in a neurotoxic amyloid intermediate of Alzheimer's β-amyloid. *Nat. Struct. Mol. Biol.* **14**, 1157–1164 (2007).
75. M. Ahmed et al., Structural conversion of neurotoxic amyloid-beta(1–42) oligomers to fibrils. *Nat. Struct. Mol. Biol.* **17**, 561–567 (2010).
76. D. Huang et al., Antiparallel β-sheet structure within the C-terminal region of 42-residue Alzheimer's amyloid-β peptides when they form 150-kDa oligomers. *J. Mol. Biol.* **427**, 2319–2328 (2015).
77. H. A. Scheidt, I. Morgado, D. Huster, Solid-state NMR reveals a close structural relationship between amyloid-β protofibrils and oligomers. *J. Biol. Chem.* **287**, 22822–22826 (2012).
78. T. Doi et al., Solid-state NMR analysis of the β-strand orientation of the protofibrils of amyloid β-protein. *Biochem. Biophys. Res. Commun.* **428**, 458–462 (2012).
79. W. M. Tay, D. Huang, T. L. Rosenberry, A. K. Paravastu, The Alzheimer's amyloid-β(1–42) peptide forms off-pathway oligomers and fibrils that are distinguished structurally by intermolecular organization. *J. Mol. Biol.* **425**, 2494–2508 (2013).
80. W. Hoyer, C. Grönwall, A. Jonsson, S. Ståhl, T. Härd, Stabilization of a beta-hairpin in monomeric Alzheimer's amyloid-beta peptide inhibits amyloid formation. *Proc. Natl. Acad. Sci. U.S.A.* **105**, 5099–5104 (2008).
81. A. Sandberg et al., Stabilization of neurotoxic Alzheimer amyloid-beta oligomers by protein engineering. *Proc. Natl. Acad. Sci. U.S.A.* **107**, 15595–15600 (2010).
82. C. Lendel et al., A hexameric peptide barrel as building block of amyloid-β protofibrils. *Angew. Chem. Int. Ed Engl.* **53**, 12756–12760 (2014).
83. L. Yu et al., Structural characterization of a soluble amyloid beta-peptide oligomer. *Biochemistry* **48**, 1870–1877 (2009).
84. S. Ciudad et al., Aβ(1–42) tetramer and octamer structures reveal edge conductivity pores as a mechanism for membrane damage. *Nat. Commun.* **11**, 3014 (2020).
85. M. Serra-Batiste et al., Aβ42 assembles into specific β-barrel pore-forming oligomers in membrane-mimicking environments. *Proc. Natl. Acad. Sci. U.S.A.* **113**, 10866–10871 (2016).
86. U. Ghosh, K. R. Thurber, W.-M. Yau, R. Tycko, Molecular structure of a prevalent amyloid-β fibril polymorph from Alzheimer's disease brain tissue. *Proc. Natl. Acad. Sci. U.S.A.* **118**, e2023089118 (2021).
87. P. J. Salveson, R. K. Spencer, A. G. Kreutzer, J. S. Nowick, X-ray crystallographic structure of a compact dodecamer from a peptide derived from Aβ16-36. *Org. Lett.* **19**, 3462–3465 (2017).
88. A. G. Kreutzer et al., A hexamer of a peptide derived from Aβ16-36. *Biochemistry* **56**, 6061–6071 (2017).
89. S. Zhang et al., A disulfide-stabilized Aβ that forms dimers but does not form fibrils. *Biochemistry* **61**, 252–264 (2022).
90. T. D. Samdin, A. G. Kreutzer, J. S. Nowick, Exploring amyloid oligomers with peptide model systems. *Curr. Opin. Chem. Biol.* **64**, 106–115 (2021).
91. A. G. Kreutzer, J. S. Nowick, Elucidating the structures of amyloid oligomers with macrocyclic β-hairpin peptides: Insights into Alzheimer's disease and other amyloid diseases. *Acc. Chem. Res.* **51**, 706–718 (2018).
92. R. K. Spencer, H. Li, J. S. Nowick, X-ray crystallographic structures of trimers and higher-order oligomeric assemblies of a peptide derived from Aβ(17–36). *J. Am. Chem. Soc.* **136**, 5595–5598 (2014).
93. A. J. Kuhn, B. S. Abrams, S. Knowlton, J. A. Raskatov, Alzheimer's disease "non-amyloidogenic" p3 peptide revisited: A case for amyloid-α. *ACS Chem. Neurosci.* **11**, 1539–1544 (2020).
94. J. S. Nowick, J. O. Brower, A new turn structure for the formation of beta-hairpins in peptides. *J. Am. Chem. Soc.* **125**, 876–877 (2003).
95. J. A. Raskatov, What Is the "Relevant" Amyloid β42 concentration? *Chembiochem* **20**, 1725–1726 (2019).
96. A. G. Kreutzer, S. Yoo, R. K. Spencer, J. S. Nowick, Stabilization, assembly, and toxicity of trimers derived from Aβ. *J. Am. Chem. Soc.* **139**, 966–975 (2017).
97. M. Ramírez-Alvarado, F. J. Blanco, L. Serrano, De novo design and structural analysis of a model beta-hairpin peptide system. *Nat. Struct. Biol.* **3**, 604–612 (1996).
98. N. H. Andersen et al., Minimization and optimization of designed beta-hairpin folds. *J. Am. Chem. Soc.* **128**, 6101–6110 (2006).
99. J. M. Anderson et al., Nascent hairpins in proteins: Identifying turn loci and quantitating turn contributions to hairpin stability. *Biochemistry* **55**, 5537–5553 (2016).
100. E. Boeri Erba, L. Signor, C. Petosa, Exploring the structure and dynamics of macromolecular complexes by native mass spectrometry. *J. Proteomics* **222**, 103799 (2020).
101. S. Tamara, M. A. den Boer, A. J. R. Heck, High-resolution native mass spectrometry. *Chem. Rev.* **122**, 7269–7326 (2022).
102. K. R. Karch, D. T. Snyder, S. R. Harvey, V. H. Wysocki, Native mass spectrometry: Recent progress and remaining challenges. *Annu. Rev. Biophys.* **51**, 157–179 (2022).
103. J. L. P. Benesch, B. T. Ruotolo, Mass spectrometry: Come of age for structural and dynamical biology. *Curr. Opin. Struct. Biol.* **21**, 641–649 (2011).
104. D. T. Snyder, S. R. Harvey, V. H. Wysocki, Surface-induced dissociation mass spectrometry as a structural biology tool. *Chem. Rev.* **122**, 7442–7487 (2022).
105. D. T. Snyder et al., Surface-induced dissociation of protein complexes on a cyclic ion mobility spectrometer. *Analyst* **146**, 6861–6873 (2021).
106. A. Sonn-Segev et al., Quantifying the heterogeneity of macromolecular machines by mass photometry. *Nat. Commun.* **11**, 1772 (2020).
107. U. Sengupta, A. N. Nilson, R. Kayed, The role of Amyloid-β oligomers in toxicity, propagation, and immunotherapy. *EBioMedicine* **6**, 42–49 (2016).
108. C. Liu et al., Out-of-register β-sheets suggest a pathway to toxic amyloid aggregates. *Proc. Natl. Acad. Sci. U.S.A.* **109**, 20913–20918 (2012).
109. Y. P. Li, A. F. Bushnell, C. M. Lee, L. S. Perlmutter, S. K. Wong, Beta-amyloid induces apoptosis in human-derived neurotypic SH-SY5Y cells. *Brain Res.* **738**, 196–204 (1996).
110. J. Krishtal, O. Bragina, K. Metsla, P. Palumaa, V. Tõugu, In situ fibrillizing amyloid-beta 1–42 induces neurite degeneration and apoptosis of differentiated SH-SY5Y cells. *PLoS One* **12**, e0186636 (2017).
111. H. Yu et al., Protective and anti-oxidative effects of curcumin and resveratrol on Aβ-oligomer-induced damage in the SH-SY5Y cell line. *J. Neurol. Sci.* **441**, 120356 (2022).
112. T. Yasumoto et al., High molecular weight amyloid β 1–42 oligomers induce neurotoxicity via plasma membrane damage. *Alzheimers. Dement.* **16**, e037546 (2020).
113. G. Guaglianone et al., Elucidating the oligomerization and cellular interactions of a trimer derived from Aβ through fluorescence and mass spectrometric studies. *ACS Chem. Neurosci.* **13**, 2473–2482 (2022).
114. E. Wesén, G. D. M. Jeffries, M. Matson Dzebo, E. K. Esbjörner, Endocytic uptake of monomeric amyloid-β peptides is clathrin- and dynamin-independent and results in selective accumulation of Aβ(1-42) compared to Aβ(1-40). *Sci. Rep.* **7**, 2021 (2017).
115. G. J. Brewer et al., Age-related intraneuronal aggregation of Amyloid-β in endosomes, mitochondria, autophagosomes, and lysosomes. *J. Alzheimers. Dis.* **73**, 229–246 (2020).
116. S. Dutta, T. S. Finn, A. J. Kuhn, B. Abrams, J. A. Raskatov, Chirality dependence of Amyloid β cellular uptake and a new mechanistic perspective. *Chembiochem* **20**, 1023–1026 (2019).
117. M. Knobloch, U. Konietzko, D. C. Krebs, R. M. Nitsch, Intracellular Abeta and cognitive deficits precede beta-amyloid deposition in transgenic arcAbeta mice. *Neurobiol. Aging* **28**, 1297–1306 (2007).
118. G. K. Gouras et al., Intraneuronal Abeta42 accumulation in human brain. *Am. J. Pathol.* **156**, 15–20 (2000).
119. A. Pensalfini et al., Intracellular amyloid and the neuronal origin of Alzheimer neuritic plaques. *Neurobiol. Dis.* **71**, 53–61 (2014).
120. P. N. Lacor et al., Synaptic targeting by Alzheimer's-related amyloid beta oligomers. *J. Neurosci.* **24**, 10191–10200 (2004).
121. E. N. Cline et al., A novel crosslinking protocol stabilizes amyloid β oligomers capable of inducing Alzheimer's-associated pathologies. *J. Neurochem.* **148**, 822–836 (2019).
122. R. J. Simpson, Staining proteins in gels with silver nitrate. *CSH Protoc.* **2007**, db.prot4727 (2007).
123. A. G. Kreutzer, S. Yoo, J. S. Nowick, Covalently stabilized triangular trimer derived from Abeta16-36. Research Collaboratory Structural *Bioinformatics (RCSB) Protein Data Bank (PDB)*. https://www.rcsb.org/structure/unreleased/8ECA. Deposited 9 January 2022.
124. A. G. Kreutzer, S. Yoo, J. S. Nowick, Covalently stabilized triangular trimer derived from Abeta16-36 with p-iodo-phenylalanine. Research Collaboratory Structural *Bioinformatics (RCSB) Protein Data Bank (PDB)*. https://www.rcsb.org/structure/unreleased/8EC9. Deposited 9 January 2022.